



## Article

# Stabilizing the Solid Electrolyte Interphase of SiO<sub>x</sub> Negative Electrodes: The Role of Fluoroethylene Carbonate in Enhancing Electrochemical Performance

Paul Maldonado Nogales <sup>1</sup>, Sangyup Lee <sup>1</sup> , Seunga Yang <sup>1</sup>, Inchan Yang <sup>2</sup> , Soen Hui Choi <sup>2</sup>, Sei-Min Park <sup>2</sup>, Jae Ho Lee <sup>3</sup>, Chan Jung Kim <sup>3</sup>, Jung-Chul An <sup>2,\*</sup> and Soon-Ki Jeong <sup>1,\*</sup>

<sup>1</sup> Department of Energy Engineering, Soonchunhyang University, Soonchunhyang-ro 22-gil, Sinchang-myeon, Asan-si 31538, Republic of Korea; maldonado@sch.ac.kr (P.M.N.); 20237450@sch.ac.kr (S.L.); tmddk1107@sch.ac.kr (S.Y.)

<sup>2</sup> Carbon Materials Research Cell, Research Institute of Industrial Science and Technology (RIST), Pohang 37673, Republic of Korea; iyang@rist.re.kr (I.Y.); hes02427@rist.re.kr (S.H.C.); smpark1@rist.re.kr (S.-M.P.)

<sup>3</sup> Battery Team, Kumyang, Busan 47028, Republic of Korea; ljh87@kyc.co.kr (J.H.L.); cj63kim@kyc.co.kr (C.J.K.)

\* Correspondence: jcan@rist.re.kr (J.-C.A.); hamin611@sch.ac.kr (S.-K.J.)

**Abstract:** This study examined the role of fluoroethylene carbonate (FEC) in stabilizing the solid electrolyte interphase (SEI) and enhancing the electrochemical performance of SiO<sub>x</sub>-based composite negative electrodes in lithium-ion batteries. Two electrolyte systems were used: 1.0 mol dm<sup>-3</sup> (M) LiPF<sub>6</sub> in a mixture of ethylene carbonate (EC) and ethyl methyl carbonate (EMC) with 0.5 wt.% VC, and 1.0 M LiPF<sub>6</sub> in a mixture of EC and EMC with 1.0 wt.% VC and 10 wt.% FEC. These systems enabled the investigation of how FEC contributes to SEI stabilization and cycling stability. FEC promotes the formation of a LiF-rich SEI layer, which mitigates volume expansion and enhances capacity retention. Additionally, the accumulation of Li<sub>2</sub>CO<sub>3</sub> and Li<sub>2</sub>O in the SEI was found to increase interfacial resistance, as observed through electrochemical impedance spectroscopy (EIS). Among the SiO<sub>x</sub> contents tested (0%, 3%, and 7.8%), the 3% SiO<sub>x</sub> content exhibited the best balance between SiO<sub>x</sub> and carbon nanotubes, resulting in improved SEI formation and enhanced electrochemical performance. These results offer insights into the optimization of electrolyte formulations for long-term cycling stability in SiO<sub>x</sub>-based lithium-ion batteries.

**Keywords:** solid electrolyte interphase; silicon oxides; lithium fluoride; fluoroethylene carbonate



**Citation:** Nogales, P.M.; Lee, S.; Yang, S.; Yang, I.; Choi, S.H.; Park, S.-M.; Lee, J.H.; Kim, C.J.; An, J.-C.; Jeong, S.-K. Stabilizing the Solid Electrolyte Interphase of SiO<sub>x</sub> Negative Electrodes: The Role of Fluoroethylene Carbonate in Enhancing Electrochemical Performance. *Batteries* **2024**, *10*, 385. <https://doi.org/10.3390/batteries10110385>

Academic Editor: Ivana Hasa

Received: 8 October 2024

Revised: 24 October 2024

Accepted: 30 October 2024

Published: 31 October 2024



**Copyright:** © 2024 by the authors. Licensee MDPI, Basel, Switzerland. This article is an open access article distributed under the terms and conditions of the Creative Commons Attribution (CC BY) license (<https://creativecommons.org/licenses/by/4.0/>).

## 1. Introduction

Reducing carbon emissions and combating climate change requires a transition to electric vehicles and renewable energy storage systems, which are critically dependent on the development of efficient and sustainable battery technologies. In this context, lithium-ion batteries (LIBs) have emerged as the dominant technology owing to their high energy density and long cycle life. Although emerging energy storage technologies, such as solid-state and metal-air batteries, are gaining attention, LIBs continue to be favored for their mature manufacturing processes, established safety features, and overall commercial viability. These advantages make LIBs a critical component in current energy storage systems, despite the development of new alternatives [1–3]. However, to meet growing energy demands, significant improvements in the performance and durability of LIBs are required. Among the promising strategies to achieve these advancements is the use of silicon-based materials as negative electrodes, given their high theoretical specific capacity (Li<sub>3.75</sub>Si = 3580 mAh g<sup>-1</sup>). Despite this potential, the practical application of Si is hindered by several challenges such as poor electrical conductivity and severe volume expansion (>300%) during lithiation and delithiation, which result in rapid capacity fading [4–7]. To overcome these challenges, SiO<sub>x</sub> (silicon oxide) has been proposed as an alternative

material because it offers a balance between capacity ( $\sim 1400 \text{ mAh g}^{-1}$ ) and cycling stability, providing better long-term performance compared to pure silicon.

However, SiO<sub>x</sub>-based negative electrodes also face challenges such as low initial Coulombic efficiency (ICE) and continuous electrolyte consumption during the formation of the solid electrolyte interphase (SEI) [8–10]. Blending SiO<sub>x</sub> with graphite at a low mass ratio to form composite negative electrodes has been proposed as an effective solution [11,12]. Various strategies have been explored to improve the cycling stability of SiO<sub>x</sub>-based negative electrodes, including the use of electrolyte additives [13–15], novel binders, pre-lithiation techniques [16], nanomaterial synthesis [5,17], and surface coatings [18]. In particular, electrolyte additives such as fluoroethylene carbonate (FEC) and vinylene carbonate (VC) have gained attention due to their ability to form a stable SEI, which can mitigate the negative effects of volume expansion and improve overall battery performance [16–19]. While metallic lithium negative electrodes offer high theoretical capacity, they suffer from significant challenges such as dendrite formation, which can lead to short circuits and safety concerns, as well as poor cycling stability due to continuous SEI formation. In contrast, SiO<sub>x</sub>-based negative electrodes provide enhanced cycling stability and significantly reduce the risk of dendrite formation. This makes them a promising alternative for improving the long-term performance and safety of lithium-ion batteries. Recent studies on multi-anion electrolytes and high-entropy systems further suggest that optimized SEI layers, such as LiF-rich SEI, can accelerate ion diffusion and suppress dendrite growth, improving battery durability [20–22]. Despite these advancements, achieving long-term cycling stability for SiO<sub>x</sub>-based electrodes remains challenging. There is still a gap in understanding the detailed role of FEC in enhancing SEI stability and how different electrolyte formulations interact with SiO<sub>x</sub> electrodes over extended cycling. Addressing this gap is crucial for advancing the development of more durable lithium-ion batteries. Therefore, a deeper understanding of the interactions between SiO<sub>x</sub>-based negative electrodes and various electrolyte formulations is crucial. Specifically, the role of FEC in stabilizing the SEI and improving electrochemical performance requires further exploration.

This study aimed to address these gaps by systematically investigating the electrochemical performance and SEI formation of graphite/SiO<sub>x</sub> composite electrodes with varying SiO<sub>x</sub> contents (0%, 3%, and 7.8%) in the presence of FEC and VC additives. The findings of this research provide valuable insights into the optimization of SiO<sub>x</sub>-based composite negative electrodes for enhanced performance and cycling stability in lithium-ion batteries.

## 2. Materials and Methods

### 2.1. Electrode Materials

Artificial graphite was prepared through a sequential process of pulverization, graphitization, and carbon coating, using needle coke derived from coal. The needle coke was obtained from POSCO MC MATERIALS (Jeonnam, Republic of Korea) and pulverized to an average particle size of 10  $\mu\text{m}$ . The pulverized coke was then graphitized at 3000 °C using an induction furnace (IT-GTV-200-200-3000, Linn, Germany). After graphitization, the material underwent a carbon coating process using coal tar as the carbon source in a nitrogen atmosphere at 1200 °C. SiO<sub>x</sub> was sourced from POSCO SILICON SOLUTION (Gyeongsang, Republic of Korea) and used without further treatment. According to the certificate of analysis, SiO<sub>x</sub> has an initial Coulombic efficiency of ~82% and a capacity of  $\sim 1400 \text{ mAh g}^{-1}$ . Negative electrodes were prepared using different combinations of active materials. The first sample (G-SC-85) consisted of graphite and Super C, with 95.60% active material. The other samples contained 96.15% active material, including G-SC (graphite and super C), G-3Si-SC (3% SiO<sub>x</sub>), G-3Si-SC-CNT (3% SiO<sub>x</sub> and CNT), G-7.8Si-SC (7.8% SiO<sub>x</sub>), and G-7.8Si-SC-CNT (7.8% SiO<sub>x</sub> and CNT). The electrodes were fabricated using graphite and SiO<sub>x</sub> as active materials. Super-C and CNT served as conductive agents, which were mixed with styrene-butadiene rubber and carboxymethyl cellulose as binders. The mixing ratio of the active material, conductive agent, and binder was 96:1:3. The

active materials were mixed with polyvinylidene fluoride (PVDF) binder in N-methyl-2-pyrrolidone (NMP) to form a slurry. This slurry was coated onto 18- $\mu\text{m}$ -thick copper foil and dried to a thickness of 65  $\mu\text{m}$  for all samples, except for G-SC-85 (85  $\mu\text{m}$ ). The electrodes were dried in a vacuum oven at 80 °C for 12 h. After drying, 13 mm diameter disks were punched and stored in a dry box. The coating surface density was 7.2 g m<sup>-2</sup> for all samples except G-SC-85 (10.1 g m<sup>-2</sup>), allowing for the examination of the impact of increased active material loading.

## 2.2. Electrolyte Preparation

Two electrolytes were used: L2:8-VC, consisting of 1 mol dm<sup>-3</sup> (M) LiPF<sub>6</sub> in a 2:8 (*v/v*) mixture of ethylene carbonate (EC) and ethyl methyl carbonate (EMC) with 0.5 wt.% VC, and L3:7-VCFEC, containing 1 M LiPF<sub>6</sub> in a 3:7 (*v/v*) mixture of EC and EMC with 1.0 wt.% VC and 10 wt.% FEC. Electrolytes were obtained from Guotai-Huarong GTHR Chemical and PuriEL Soulbrain Corporation. All electrolytes were stored in an argon-filled glove box (SK-G1200, Three-Shine Inc., Daejeon, Republic of Korea) at a dew point of −70 °C to maintain low moisture levels and ensure their integrity.

## 2.3. Material Characterizations

After the third cycle in the Li<sup>+</sup> extraction state, the negative electrodes were carefully removed from the coin cells and rinsed with the EMC for 10 min to remove any residual electrolyte. The samples were then dried under vacuum at room temperature for 10 h. To prevent exposure to oxygen and moisture, the dried samples were sealed in aluminum bags and transferred to the X-ray photoelectron spectroscopy (XPS) load-lock chamber. XPS analysis was performed using a K-Alpha XPS instrument (Thermo Fisher Scientific, Waltham, MA, USA) with an Al K $\alpha$  source (1486.6 eV, 3 mA, 12 kV). Argon etching was conducted every 100 s for ten cycles. The spectra were analyzed using Thermo Avantage v5.9912 software with peak fitting following Powell's method using a dual Lorentzian-Gaussian function. The C 1s region was calibrated using a hydrocarbon peak at 284.4 eV as an internal standard. The sputtering rate, calibrated on tantalum, was approximately 3 nm min<sup>-1</sup>.

## 2.4. Electrochemical Measurements

The electrochemical properties of the electrodes were evaluated using 2032-type coin cells configured as half-cells, consisting of a testing electrode, a 16- $\mu\text{m}$ -thick separator (Celgard A273, Celgard Korea, Inc., Chungbuk, Republic of Korea), a 500- $\mu\text{m}$ -thick lithium foil counter electrode (Honjo Metal Co., Osaka, Japan), and 100  $\mu\text{L}$  of electrolyte solution. The cells were assembled in a glove box filled with pure Ar to avoid moisture and oxygen contamination and rested for 10 h to ensure proper wetting of the electrode and separator. The N/P ratio, representing the capacity ratio of the negative to the positive electrode, was 42.18 for G-SC-85, 64.99 for G-SC, 61.70 for G-3Si-SC and G-3Si-SC-CNT, and 55.18 for G-7.8Si-SC and G-7.8Si-SC-CNT, carefully controlled for balanced cell performance. Rate capability tests were conducted at 0.1, 1, 3, 5, 10, and back to 0.1 C rates, followed by 100 cycles at 1 C between 0.005 and 1.5 V using a battery test system (WBCS 3000, Wonatech Co., Ltd., Seoul, Republic of Korea). Electrochemical impedance spectroscopy (EIS) measurements were performed using a three-electrode cell configuration, as shown in Figure 1, with lithium metal foil serving as both the counter and reference electrodes and the prepared SiO<sub>x</sub>-based electrode as the working electrode. Measurements were taken with an impedance analyzer (ZIVE-MP2A, ZIVE Lab., Seoul, Republic of Korea) at 25 °C in a temperature-controlled chamber. The impedance spectra were recorded after 3 cycles during the discharge process at equilibrium voltages of 0.7 and 0.2 V over a frequency range from 1 mHz to 1000 kHz, with a signal amplitude of 15 mV. The experimental spectra were modeled and fitted using equivalent circuit analogs with Zview v4 software (Scribner Assoc.).

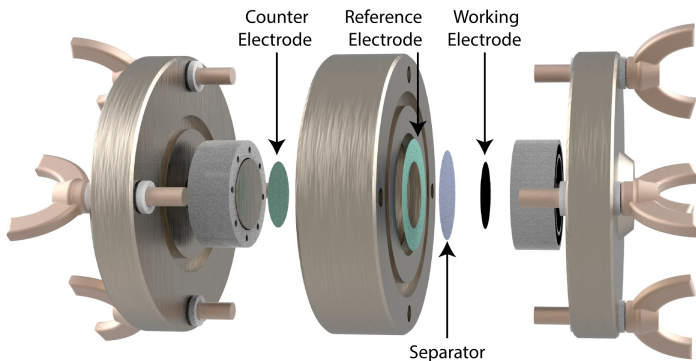


**Figure 1.** Schematic representation of the three-electrode cell configuration.

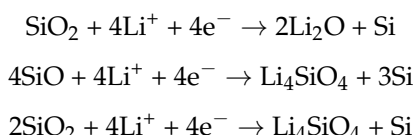
### 3. Results and Discussion

#### 3.1. Performance and Stability of SiO<sub>x</sub>-Based Electrodes

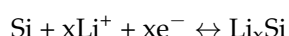
The electrochemical properties of the CR2032 coin cells, including the charge-discharge profiles, rate capability, and cycling performance, were investigated using different electrolytes. Figure 2a,b present the initial charge-discharge profiles of SiO<sub>x</sub> composite electrodes tested at 0.1 C in the voltage range of 0.005 to 1.5 V, using L2:8-VC and L3:7-VCFEC electrolytes, respectively. The initial discharge capacity and initial Coulombic efficiency (ICE) are summarized in Figure 2c,d, respectively. During the first charge (lithiation), the capacity observed above 0.2 V is primarily due to the formation of the solid electrolyte interphase (SEI) layer. Below 0.2 V, the capacity reflects an alloying reaction between lithium and silicon or graphite [23,24]. Notably, the L3:7-VCFEC electrolyte exhibited a higher capacity >0.2 V compared to L2:8-VC, suggesting that the additives in L3:7-VCFEC promoted the formation of a more robust SEI layer. This, in turn, contributes to a slightly higher initial discharge capacity. The formation of a robust SEI can act as a barrier against volume expansion, which is commonly observed in Si-based electrodes, thereby reducing SEI formation during cycling [25].

To further explore the electrochemical behavior, the reactions in the different voltage regions were categorized as follows [26]:

- Formation of Organic SEI Layer at >0.2 V.



- Reversible alloying reaction at <0.2 V.



To eliminate the influence of electrode thickness on electrochemical performance, a control sample (G-SC-85) with a standard thickness of 85 µm was fabricated. This sample exhibited initial discharge capacities of 268 and 310 mAh g<sup>-1</sup> with the L2:8-VC and L3:7-VCFEC electrolytes, respectively. In contrast, a thinner electrode (G-SC) with a reduced thickness of 65 µm showed higher initial discharge capacities of 307 and 335 mAh g<sup>-1</sup> under the same electrolyte conditions. These results suggest that thinner electrodes enhance the electrochemical performance by reducing diffusion limitations and improving active material utilization. Consequently, all subsequent electrodes were fabricated with a thickness of 65 µm to ensure that variations in electrochemical activity were due to interactions with the electrolytes rather than differences in physical dimensions.

As shown in Figure 2c, the samples with a higher SiO<sub>x</sub> content exhibited a greater initial discharge capacity. This higher capacity is attributed to the greater electrochemical activity of the non-stoichiometric SiO<sub>x</sub> phase as a negative electrode material [9]. However,

increasing the SiO<sub>x</sub> content to 7.8% resulted in a decrease in the ICE to 87% and 90% for the G-7.8Si-SC sample, which agrees with the findings of Zhao et al. [8–10]. The incorporation of carbon nanotubes (CNTs) in the G-7.8Si-SC-CNT sample slightly increased the ICE compared to that of the G-7.8Si-SC sample, likely due to the improved flexibility and porosity provided by CNTs, which enhanced contact with the electrolyte [27,28]. Conversely, samples with a lower SiO<sub>x</sub> content demonstrated improved SEI properties, leading to a higher ICE of 95%. The highest ICE values were recorded for the G-SC-85, G-SC, G-3Si-SC, and G-3Si-SC-CNT samples despite their lower initial discharge capacities. These observations suggest that optimizing the SiO<sub>x</sub> content is crucial for balancing the capacity and ICE, offering valuable insights for future studies on SEI formation mechanisms.

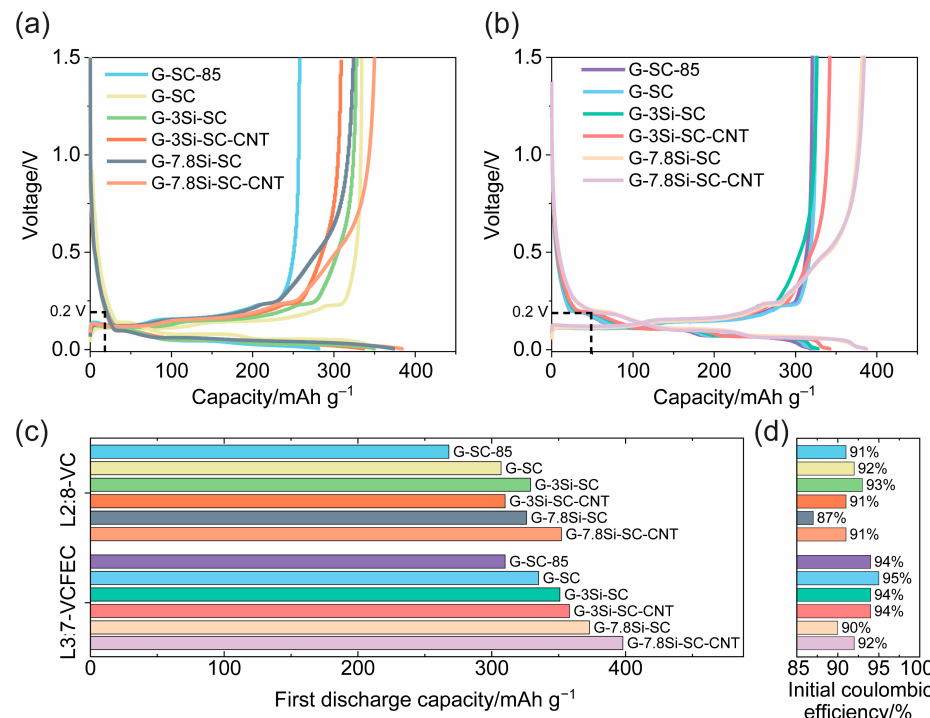


**Figure 2.** First charge-discharge profiles of all electrodes in (a) L2:8-VC and (b) L3:7-VCFEC electrolytes. (c) First discharge capacity values of all electrodes and (d) their corresponding initial Coulombic efficiencies.

### 3.2. High-Rate Performance and Cycling Durability

The rate capabilities and cycling performances of all the samples are shown in Figure 3a,b. During the initial three cycles, cells cycled with the L3:7-VCFEC electrolyte exhibited stable performance. In contrast, the L2:8-VC electrolyte showed a slight drop in discharge capacity. Further rate capability testing did not display any capacity overshoot; instead, it exhibited a lower capacity, which suggests the formation of a relatively weak but functionally stable SEI layer. For instance, the G-7.8Si-SC-CNT sample maintains a discharge capacity of around 145 mAh g<sup>-1</sup> even as the current density increases from 0.1 to 10 C. In contrast, cells cycled with L3:7-VCFEC show a significant capacity overshoot at higher current densities (3, 5, and 10 C), followed by a sharp drop, indicating a limited rate capability and poor recovery. This irregular behavior suggests the formation of Li<sub>2</sub>O from SiO<sub>2</sub> and a mechanically unstable SEI layer, as previously observed for graphite electrodes [29]. At high rates, the SEI in these samples may exhibit low mechanical strength and poor ion diffusivity, requiring several cycles for stabilization. This phenomenon was evident in the G-3Si-SC and G-SC samples, where the initial capacity peaks at 3 and 5 C stabilized after a few cycles. Upon returning to 0.1 C and later to 1 C, the capacity is fully recovered, demonstrating structural stability across all samples, independent of the electrolyte used.

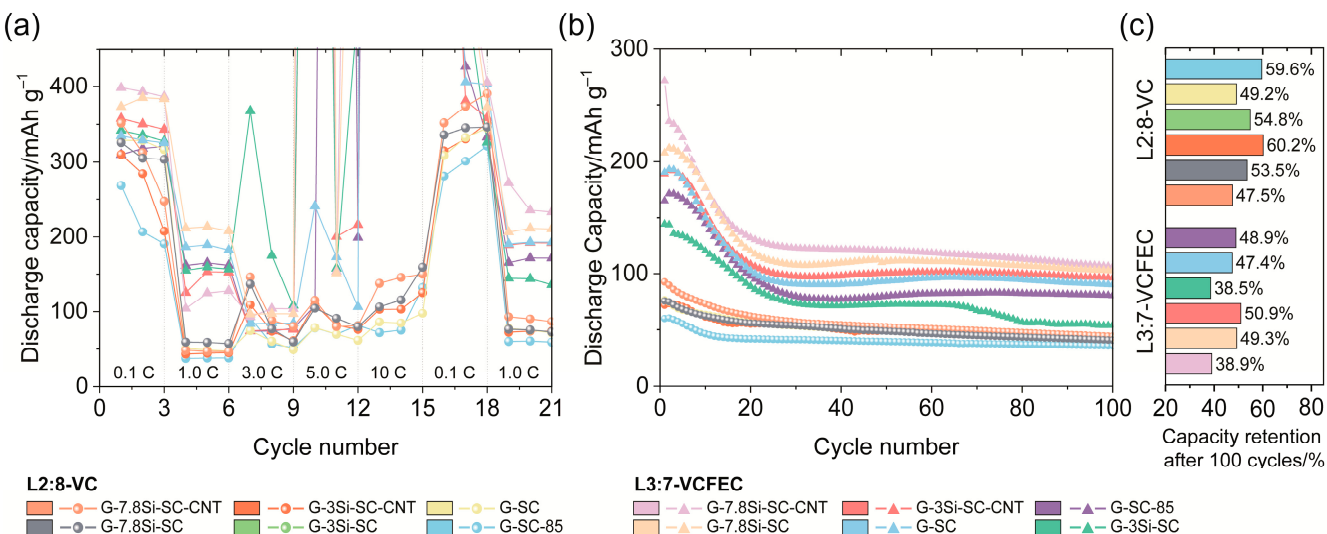


**Figure 3.** (a) Rate capability at different current densities in both electrolytes. (b) Cycling performance and (c) capacity retention after 100 cycles in the L2:8-VC and L3:7-VCFEC electrolytes.

The cycling performance post-rate capability tests are shown in Figure 3b. All samples exhibited a capacity drop during the first 30 cycles, likely due to SEI stabilization [27]. For cells tested with the L3:7-VCFEC electrolyte, an initial capacity increase was observed over the first few cycles. This increase can be attributed to the gradual activation of electrochemical reactions and SEI formation at lower rates. Capacity overshoot during previous high-rate cycling may have hindered complete SEI development, requiring further stabilization at 1C, which contributed to the capacity rise. After 100 cycles, the G-7.8Si-SC-CNT sample maintains relatively high discharge capacities of 48 and 104 mAh g<sup>-1</sup> under the L2:8-VC and L3:7-VCFEC electrolytes, respectively. A notable case is the G-3Si-SC-based battery, which exhibited capacity decay near the 70th cycle, likely due to mechanical degradation of SiOx caused by volume changes, loss of electrical connectivity, and SEI breakdown. However, this sample also exhibited the lowest capacity retention in both electrolytes, indicating reduced stability during extended cycling. In contrast, as shown in Figure 3c, the G-3Si-SC-CNT electrodes demonstrated superior stability, with capacity retention values of 60.2% and 50.9% in the L2:8-VC and L3:7-VCFEC electrolytes, respectively. The improved retention is due to the well-dispersed Si and CNT, which serve as conductive enhancers and structural stabilizers, preserving electrical connectivity and structural integrity throughout the cycling process. The homogeneous CNT distribution within the SiOx matrix not only improves the electrical conductivity but also mitigates volume expansion during cycling, maintaining electrode integrity and enhancing capacity retention. This study highlights the importance of further investigation into the influence of CNT content and electrolyte additives on SEI stability, which is critical for understanding the long-term performance of Si-based electrodes.

### 3.3. Electrochemical Impedance Spectroscopy Analysis

To further investigate the electrochemical conductivity of the electrodes, EIS measurements were conducted after three cycles at 0.7 V (Figure 4a,c) and 0.2 V (Figure 4b,d) in the lithiated state, corresponding to SEI formation and the Li-Si alloying reaction, respectively. The Nyquist plots reveal three distinct features: two semicircles in the high- and middle-frequency regions and a straight tail in the low-frequency region. The high-frequency intercept on the x axis represents the solution resistance ( $R_S$ ), whereas the two semicircles correspond to the SEI resistance ( $R_{SEI}$ ) and charge-transfer resistance ( $R_{CT}$ ). The low-frequency tail indicates the Warburg impedance ( $W$ ) associated with lithium diffusion in the solid phase.  $R_{SEI}$  influences ion mobility within the SEI layer, whereas  $R_{CT}$  governs

charge transfer at the electrode–electrolyte interface. The impedance spectra were fitted to an equivalent circuit model, as shown in the inset of Figure 4a.

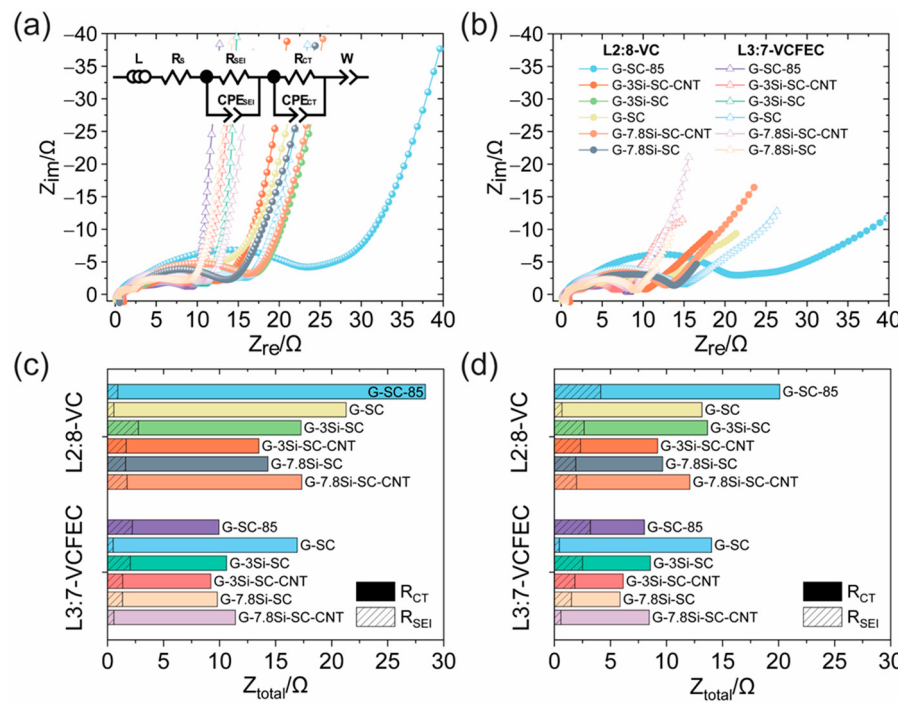


**Figure 4.** EIS measurements at (a) 0.7 and (b) 0.2 V. Summary of  $R_{SEI}$  and  $R_{CT}$  values at (c) 0.7 and (d) 0.2 V.

The combined resistances  $R_{SEI}$  and  $R_{CT}$  are summarized as  $Z_{total}$  in Figure 4c,d. As shown in Figure 4a,b, the cells with the L3:7-VCFEC electrolyte exhibited smaller semi-circles than those with L2:8-VC, suggesting the formation of a LiF-rich SEI layer from FEC decomposition, which enhanced the ionic conductivity and mechanical stability [30]. This reduced overall resistance is reflected in the improved electrochemical performance observed in the charge-discharge profiles (Figure 2b) and discharge capacity retention after 100 cycles (Figure 3b). Among all the samples, the G-3Si-SC-CNT electrode exhibited the lowest  $Z_{total}$  and interfacial resistance, indicating the formation of a highly conductive and stable SEI layer that significantly improved the charge transfer and overall conductivity.

At 0.2 V, the G-7.8Si-SC and G-3Si-SC-CNT samples displayed the lowest total resistance, suggesting that a dense and uniform SEI layer formed during discharge. This stable layer was associated with the Si-Li alloying reaction and contributed to the higher capacity retention observed after 100 cycles (Figure 3c). These results demonstrate that the combination of SiO<sub>x</sub> and CNT in the electrode structure not only enhances the structural stability and electronic conductivity but also facilitates continuous electron transport pathways. The uniform distribution of CNTs within the SiO<sub>x</sub> matrix minimized the interfacial resistance and optimized the charge-transfer efficiency. This study underscores the significance of characterizing the SEI layer to better understand the relationship between interfacial resistance and cycling stability of Si-based electrodes.

### 3.4. XPS Examination of SEI Formation

The influence of the SEI layer formed during cycling on both the pre-cycled and post-cycled electrodes after 3 and 100 cycles was analyzed using XPS. Figure S1 presents the C1s spectra and Figure 5 shows the Si 2p spectra of the pristine samples, providing baseline information on the chemical state before cycling. The C1s spectra (Figure S1) display a reference C-C peak at ~284.4 eV, which is attributed to adventitious carbon contamination. Additional peaks corresponding to the C = O, C-O-C, and C-OH bonds were observed

with higher intensities in the CNT-containing samples, suggesting an enhanced surface interaction with the electrolyte. The Si 2p spectra (Figure 5) show two broad bands at 99 and 103 eV, deconvoluted into five subpeaks at 98.9, 99.5, 100.9, 102.8, and 103.6 eV, corresponding to the spin-orbit components of Si 2p<sub>3/2</sub> and Si 2p<sub>1/2</sub>, as well as SiO<sub>0.5</sub>, SiO<sub>1.5</sub>, and SiO<sub>2</sub>, respectively. The O 1s spectrum (Figure S2) further aids in peak identification. For example, the 532.3 eV peak in the O 1s spectrum corresponds to the SiO<sub>1.5</sub> peak at 102.8 eV in the Si 2p spectrum, confirming the presence of various SiO<sub>x</sub> oxidation states.

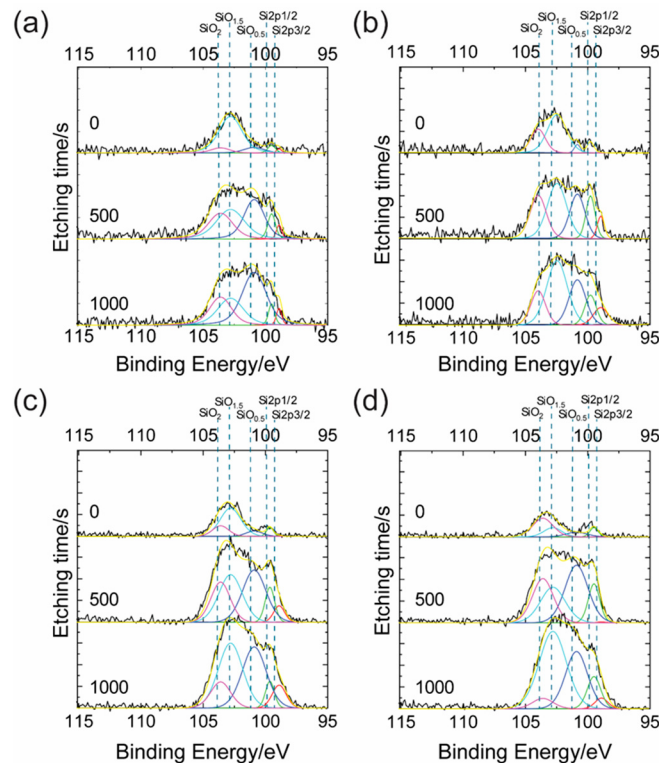


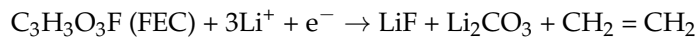
**Figure 5.** XPS elemental composition of Si 2p in pristine samples before cycling: (a) G-3Si-SC, (b) G-3Si-SC-CNT, (c) G-7.8Si-SC, and (d) G-7.8Si-SC-CNT.

In the SiO<sub>x</sub>-containing samples, the predominant O 1s peak at 533 eV corresponded to SiO<sub>2</sub>, indicating its significant presence in the SEI, which provided mechanical stability and acted as a buffer against volume changes during cycling. Peaks at 532.3 eV are attributed to SiO<sub>1.5</sub> and SiOH, while smaller peaks at 530.8 and 529.8 eV correspond to SiO<sub>0.5</sub> and C-O bonds. In samples without SiO<sub>x</sub>, peaks at 531.97 eV (C=O and C-O-C) and 533.34 eV (C-OH and O-C=O) are related to the binder in the composite. These results suggest that the SiO<sub>x</sub> phase, comprising SiO<sub>x</sub> ( $x = 0.5, 1.5$ , and 2), plays a critical buffering role during lithium insertion and extraction. Understanding the relationship between SiO<sub>x</sub> reduction and electrochemical performance is crucial for elucidating the SEI formation mechanisms and their impact on cycling stability.

To evaluate the changes in the elemental composition after 3 and 100 cycles, the presence of Si and Li in the composite was analyzed using XPS. Figures S3 and S5 show the Si 2p spectra, whereas Figures S4 and S6 present the Li 1s spectra, revealing the evolution of the SEI composition during cycling. The Si 2p spectra show peaks at 98.9 and 99 eV for Si 2p<sub>3/2</sub> and Si 2p<sub>1/2</sub>, and at 100.9, 102.8, and 103.6 eV for LixSi, SiO<sub>1.5</sub>, and SiOxFy composites, respectively [31]. In Figure S3, Si binding energy is not detected on the surface but appears after 500 s of Ar etching, indicating the presence of Li silicates and Li<sub>2</sub>O in the underlying layer, likely formed from the lithiation of the oxidized Si surface (e.g., SiO<sub>0.5</sub>, SiO<sub>1.5</sub>, and SiOxFy) [32]. After 100 cycles (Figure S5), the G-3Si-SC and G-3Si-SC-CNT

samples showed no Si 2p peaks, suggesting the formation of a thicker non-Si SEI layer (e.g., LiF, Li<sub>2</sub>O, and Li<sub>2</sub>CO<sub>3</sub>) that obscured the Si signal, indicating substantial SEI growth.

In Figures S4 and S6, the Li 1s spectra show a broad peak between 56 and 58 eV, with subpeaks at 54.02, 56.06, and 56.82 eV, corresponding to Li<sub>2</sub>O, Li<sub>2</sub>CO<sub>3</sub>, and LiF, respectively. These subproducts result from the decomposition of electrolyte components such as EC, EMC, VC, FEC, and LiPF<sub>6</sub>. In the L2:8-VC electrolyte, LiF formation was detected at a lower level than that in the L3:7-VCFEC electrolyte, which contained FEC. The increased presence of LiF in L3:7-VCFEC is attributed to FEC's reductive decomposition of FEC, which enhances the mechanical stability and ionic conductivity of the SEI, thereby improving the electrochemical performance. The primary chemical reaction is described as follows:

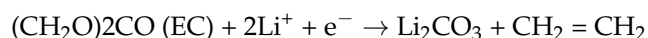


The formation of a thick LiF-rich SEI layer on the electrode surface suggests improved structural stability and enhanced cycling performance, particularly with the L3:7-VCFEC electrolyte. This study underscores the importance of exploring the impact of SEI thickness on charge transfer resistance, which is vital for optimizing SEI composition and improving long-term performance.

### 3.5. Analysis of the SEI Layer Stability

As shown in Table 1, LiF formation was observed in all samples, with the G-SC sample showing significantly higher quantities after both 3 and 100 cycles, indicating consistent LiF formation throughout the cycling (Figure 6a). This stability is attributed to the absence of Si, which prevents issues such as electrode cracking, expansion, and continuous SEI exfoliation. In the G-3Si-SC sample, a high LiF content was detected only after 100 cycles, suggesting delayed SEI formation due to the initial SiO<sub>x</sub>-electrolyte interactions, which stabilized the SEI by incorporating LiF at a later stage. The G-SC-85 sample exhibited distinct behavior, with a significantly higher percentage of Li<sub>2</sub>CO<sub>3</sub> (57%), which may explain the increase in Z<sub>total</sub> (Figure 4c,d) and the low first discharge capacity (Figure 2c). The presence of Li<sub>2</sub>CO<sub>3</sub> suggests low mechanical strength and surface energy, which affects SEI formation, composition, and stability, leading to SEI dissolution and side reactions at the negative electrode.

Similarly, the G-SC electrode in the L3:7-VCFEC electrolyte system exhibits an increase in Li<sub>2</sub>CO<sub>3</sub> (Figure 6d), highlighting the impact of the additives on Li<sub>2</sub>CO<sub>3</sub> formation. Although electrolyte solvents and additives influence the electrochemical reactions, they do not completely suppress them, resulting in higher Li<sub>2</sub>CO<sub>3</sub> concentrations. The primary reaction leading to Li<sub>2</sub>CO<sub>3</sub> formation is as follows:



The decomposition of FEC also contributes to Li<sub>2</sub>CO<sub>3</sub> formation. Impedance analysis after cycling (Figure 4c,d) confirmed that a high Li<sub>2</sub>CO<sub>3</sub> content was associated with an increased Z<sub>total</sub>, indicating higher SEI resistivity. As shown in Table 2, G-SC-85 exhibited significant LiF formation after 3 cycles, which decreased to less than a quarter after 100 cycles with a concurrent increase in Li<sub>2</sub>CO<sub>3</sub>, indicating considerable surface instability over extended cycling. This behavior is similar to that observed in the L2:8-VC system, where the Li<sub>2</sub>CO<sub>3</sub> content increased owing to electrolyte-electrode reactions.

In contrast, the G-7.8Si-SC-CNT and G-3Si-SC-CNT samples maintained high and stable LiF levels over 3 and 100 cycles (Figure 6e,f), suggesting that FEC and CNT helped preserve the electrode stability, as evidenced by the initial discharge capacity, although this was not sustained after 100 cycles. The presence of Li<sub>2</sub>CO<sub>3</sub> byproducts in the G-7.8Si-SC-CNT sample may have affected its long-term cycling performance. Samples containing SiO<sub>x</sub> generally exhibited a significant Li<sub>2</sub>CO<sub>3</sub> content, except for the G-3Si-SC-CNT sample, which remained stable and slightly decreased after 100 cycles (Figure 6b,e). This suggests

that variations in the  $\text{Li}_2\text{CO}_3$  content directly influence cell stability, as observed in the capacity retention (Figure 3b,c) and EIS tests (Figure 4c,d).

**Table 1.** Atomic content percentages of  $\text{SiO}_2$ ,  $\text{SiO}_{1.5}$ ,  $\text{SiOH}$ ,  $\text{SiO}_{0.5}$ ,  $\text{LixSi}$ ,  $\text{LiF}$ ,  $\text{Li}_2\text{O}$ , and  $\text{Li}_2\text{CO}_3$  compounds identified before cycling, after 3 cycles, and after 100 cycles in the L2:8-VC electrolyte.

L2:8-VC	$\text{SiO}_2$	$\text{SiOxFy}$		$\text{SiO}_{1.5}$		$\text{SiOH}$		$\text{SiO}_{0.5}$	$\text{LixSi}$		$\text{LiF}$			$\text{Li}_2\text{O}$			$\text{Li}_2\text{CO}_3$		
		Before	At 3 cy.	At 100 cy.	Before	At 3 cy.	At 100 cy.		Before	At 3 cy.	At 100 cy.	Before	At 3 cy.	At 100 cy.	Before	At 3 cy.	At 100 cy.	Before	At 3 cy.
G-SC-85	0	0	0	0	0	0	0	0	0	0	42.6	39.1	0	0	3.1	0	57.4	57.8	
G-SC	0	0	0	0	0	0	0	0	0	77	98.6	0	0	0	0	22.5	1.3		
G-3Si-SC	46.4	11.6	6.9	52.7	12.9	9.9	0.88	0	0	0	42	62.3	0	0	8.1	0	18.2	8.4	
G-3Si-SC-CNT	66.1	13.36	12	31.1	26.8	0.4	2.7	0	0	0	45.1	46.2	0	13.5	24.85	0	1.4	16.5	
G-7.8Si-SC	58.87	4.15	7.9	37.36	33.8	4.6	3.75	0.25	2.7	0	49	43	0	0	13.4	0	12.4	28.3	
G-7.8Si-SC-CNT	50.87	3.9	2.7	46.16	13.4	10.3	2.96	1.85	0	0	65.8	32.8	0	7.94	28.7	0	13.1	25.7	

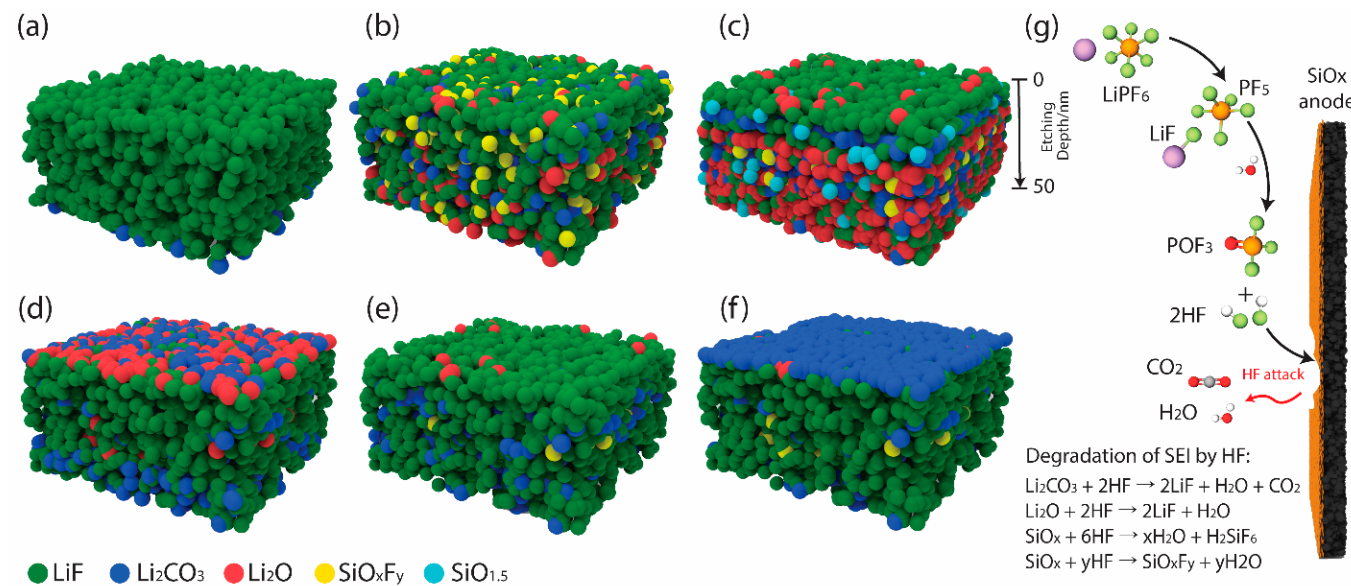
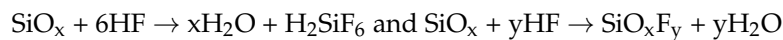


**Figure 6.** Ideal schematic representation of SEI layers based on XPS results for samples: (a) G-SC, (b) G-3Si-SC-CNT, and (c) G-7.8Si-SC-CNT in the L2:8-VC electrolyte, and (d) G-SC, (e) G-3Si-SC-CNT, and (f) G-7.8Si-SC-CNT in the L3:7-VCFEC electrolyte after 100 cycles. (g) Schematic illustration of HF formation and SEI degradation by HF.

In addition to  $\text{Li}_2\text{CO}_3$ , electrochemically inactive  $\text{Li}_2\text{O}$  and  $\text{LixSi}$  alloys within the SEI impede electron transfer and Li-ion mobility, as noted by Jiao et al. Comparing Tables 1 and 2, the  $\text{Li}_2\text{O}$  content was higher in the L2:8-VC electrolyte (Figure 6b,c), correlating with a lower discharge capacity. This effect is more pronounced at high current densities, where the SiO<sub>x</sub> negative electrode shows an unstable rate performance, particularly with the L3:7-VCFEC electrolyte. Nguyen et al. also reported that acid etching caused by hydrofluoric acid (HF) from the electrolyte salt degrades the cell stability in negative electrodes with a higher oxygen content [33,34]. HF-related reactions are as follows:



These reactions indicate that HF formed from the electrolyte salt etches the SiO<sub>x</sub> negative electrode material, resulting in various silicon fluorides (e.g.,  $\text{H}_2\text{SiF}_6$  and  $\text{SiO}_x\text{F}_y$ ), water, and  $\text{CO}_2$ , along with the potential release of Si, depending on the stoichiometry of

the oxide layer. HF also decomposes SEI constituents, such as  $\text{Li}_2\text{CO}_3$  and  $\text{Li}_2\text{O}$ , forming  $\text{CO}_2$  and water, which produce electrolyte byproducts (Figure 6g).

**Table 2.** Atomic content percentages of  $\text{SiO}_2$ ,  $\text{SiO}_{1.5}$ ,  $\text{SiOH}$ ,  $\text{SiO}_{0.5}$ ,  $\text{LixSi}$ ,  $\text{LiF}$ ,  $\text{Li}_2\text{O}$ , and  $\text{Li}_2\text{CO}_3$  compounds identified before cycling, after 3 cycles, and after 100 cycles in the L3:7-VCFEC electrolyte.

L3:7-VCFEC	$\text{SiO}_2$	$\text{SiOxFy}$			$\text{SiO}_{1.5}$			$\text{SiOH}$			$\text{SiO}_{0.5}$			$\text{LixSi}$			$\text{LiF}$			$\text{Li}_2\text{O}$			$\text{Li}_2\text{CO}_3$		
		Before	At 3 cy.	At 100 cy.	Before	At 3 cy.	At 100 cy.	Before	At 3 cy.	At 100 cy.	Before	At 3 cy.	At 100 cy.	Before	At 3 cy.	At 100 cy.	Before	At 3 cy.	At 100 cy.	Before	At 3 cy.	At 100 cy.	Before	At 3 cy.	At 100 cy.
G-SC-85	0	0	0	0	0	0	0	0	0	0	0	89.9	24.1	0	0.76	14.6	0	9.3	61.2	0	0	0	0	0	0
G-SC	0	0	0	0	0	0	0	0	0	0	0	45	70.8	0	0	8.8	0	54	20.3	0	0	0	0	0	0
G-3Si-SC	46.4	4.11	2.7	52.7	16.65	0	0.88	0.08	0	0	65	61	0	0.17	0	0	0	12.78	16.3	0	0	0	0	0	0
G-3Si-SC-CNT	66.1	6.8	1.6	31.1	0.22	0.95	2.7	0.07	0	0	80.16	82.9	0	0	2.5	0	0	13.44	12	0	0	0	0	0	0
G-7.8Si-SC	58.87	3.6	5.2	37.36	26.16	2.8	3.75	0.57	1.1	0	52.9	56.3	0	0	3.7	0	0	13.22	23.3	0	0	0	0	0	0
G-7.8Si-SC-CNT	50.87	0.37	1.3	46.16	4.1	0.5	2.96	1.37	0.43	0	80	74.4	0	0.8	0	0	0	16.7	29.7	0	0	0	0	0	0

Although HF was not specifically tested in this study, its presence is likely because it is a common byproduct of commercial electrolytes containing  $\text{LiPF}_6$ . HF etching causes continuous changes in the composition and structure of the SEI layer, thereby degrading its stability. Because the SEI layer is crucial for protecting the negative electrode and facilitating ion transport, its degradation results in poor cycling stability and reduces battery performance. Therefore,  $\text{SiOx}$  negative electrodes may not be compatible with certain electrolytes, particularly those that generate HF, leading to performance loss and instability. Refining the electrolyte composition to control HF production is crucial for maintaining SEI stability, which can enhance the overall electrode performance. Tailored electrolyte formulations are the key to unlocking the potential of  $\text{SiOx}$  electrodes, offering a path for improved performance and extended battery lifespans.

The G-3Si-SC-CNT sample showed limited influence of the  $\text{SiOx}$ -HF interactions, indicating improved SEI formation and a more stable electrochemical environment. The high reversibility of active  $\text{SiOx}$  during cycling, as suggested by the low  $\text{LixSi}$  and  $\text{SiOxFy}$  contents in the XPS results, resulted in a homogeneous mixture of  $\text{LiF}$  with minimal  $\text{Li}_2\text{CO}_3$  and  $\text{Li}_2\text{O}$  (Figure 6e). This composition may enhance the lithiation–delithiation capability of the  $\text{SiOx}$  negative electrode, as a lower  $\text{LixSi}$  content indicates that less lithium is trapped in isolated  $\text{LixSi}$  particles [35,36], contributing to a higher Coulombic efficiency and discharge capacity. The synergy between  $\text{LiF}$  and  $\text{Li}_2\text{CO}_3$  in the G-3Si-SC-CNT sample provides complementary properties: high ionic conductivity ( $10^{-8}$ – $10^{-11} \text{ S cm}^{-1}$  for  $\text{Li}_2\text{CO}_3$ ), electrical insulation, high interfacial energy, and mechanical strength, collectively resulting in more stable SEI formation [37]. This suggests that stable SEI formation can be achieved through a balanced combination of SEI components with distinct characteristics rather than relying on a single SEI component.

The presence of both  $\text{LiF}$  and  $\text{Li}_2\text{CO}_3$  in the SEI prevents continuous electrolyte reduction and excessive SEI growth, which would otherwise increase cell resistance and cause capacity fading during prolonged cycling. Moreover, the SEI layer formed in the G-3Si-SC-CNT sample, unlike in the other samples, effectively protects against electrochemical decomposition and parasitic reactions, providing benefits for enhanced overall performance. These features indicate that effective stabilization of the SEI is crucial for improving the cycling life and performance of  $\text{SiOx}$ -based negative electrodes. These results suggest that a synergistic combination of all the components, including CNTs, contributes to the overall stability and performance of the cell.

#### 4. Conclusions

This study explores the effect of SEI formation on the electrochemical performance of  $\text{SiOx}$ -based composite negative electrodes using two electrolyte systems: L2:8-VC and L3:7-VCFEC. The addition of FEC to the L3:7-VCFEC electrolyte resulted in the formation

of a LiF-rich SEI, which significantly improved the stability and capacity retention of the electrodes. In contrast, the L2:8-VC electrolyte promoted consistent SEI formation under various cycling conditions. XPS analysis revealed fluctuations in the SiO<sub>2</sub>, SiO<sub>1.5</sub>, SiO<sub>0.5</sub>, SiOxFy, and Li<sub>x</sub>Si levels after cycling, indicating their role in SEI formation and their influence on electrochemical performance. The accumulation of Li<sub>2</sub>CO<sub>3</sub> and Li<sub>2</sub>O in the SEI was shown to increase interfacial resistance, as evidenced by EIS analysis, which revealed higher Z<sub>total</sub> values correlating with decreased ion mobility. This study provides detailed insights into how FEC contributes to SEI stabilization in SiOx-based electrodes, particularly by reducing the impact of volume expansion and improving cycling stability. The findings suggest that FEC plays a role in forming a LiF-rich SEI layer, which may enhance the overall performance of lithium-ion batteries during long-term cycling. Among the SiOx contents tested (0%, 3%, and 7.8%), the 3% SiOx content demonstrated the best balance between SiOx and CNTs, leading to enhanced SEI formation and improved electrochemical performance. Further exploration of electrolyte formulations and additives such as FEC and VC may provide additional insights into enhancing SEI stability and improving the cycling performance of SiOx-based lithium-ion batteries.

**Supplementary Materials:** Supporting Information can be downloaded from <https://www.mdpi.com/article/10.3390/batteries10110385/s1>. Figure S1. XPS elemental composition of C 1s of pristine samples before cycling: (a) G-SC-85, (b) G-3Si-SC, (c) G-7.8Si-SC, (d) G-SC, (e) G-3Si-SC-CNT, and (f) G-7.8Si-SC-CNT.; Figure S2. XPS elemental composition of O 1s of pristine samples before cycling: (a) G-SC-85, (b) G-3Si-SC, (c) G-7.8Si-SC, (d) G-SC, (e) G-3Si-SC-CNT, and (f) G-7.8Si-SC-CNT.; Figure S3. XPS elemental composition of S 2p of the samples after three cycles in the L2:8-VC and L3:7-VCFEC electrolytes.; Figure S4. XPS elemental compositions of L 1s samples after three cycles in L2:8-VC and L3:7-VCFEC electrolytes.; Figure S5. XPS elemental compositions of S 2p samples after 100 cycles in L2:8-VC and L3:7-VCFEC electrolytes.; Figure S6. XPS elemental composition of Li1s of samples after 100 cycles in L2:8-VC and L3:7-VCFEC electrolytes.

**Author Contributions:** Conceptualization, P.M.N., I.Y., J.-C.A. and S.-K.J.; methodology, P.M.N., S.L., S.H.C. and I.Y.; formal analysis, P.M.N., S.Y. and S.-M.P.; investigation, P.M.N., S.Y. and I.Y.; resources, P.M.N., S.Y. and C.J.K.; data curation, P.M.N., S.L. and J.H.L.; writing—original draft preparation, P.M.N.; writing—review and editing, P.M.N. and S.-K.J.; supervision, J.-C.A. and S.-K.J.; project administration, J.-C.A. and S.-K.J.; funding acquisition, J.-C.A. and S.-K.J. All authors have read and agreed to the published version of the manuscript.

**Funding:** This study was supported by “Materials/Parts Technology Development Program (20020300)” funded by the Ministry of Trade, Industry and Energy (MOTIE) of Korea. This work was supported by the Korea Institute of Energy Technology Evaluation and Planning (KETEP) and the Ministry of Trade, Industry and Energy (MOTIE) of the Republic of Korea (No. RS-2024-00394769). This study was supported by the Soonchunhyang University Research Fund.

**Data Availability Statement:** Data is contained within the article or Supplementary Material.

**Conflicts of Interest:** Authors Jae Ho Lee and Chan Jung Kim are employed by the Kumyang. The remaining authors declare that the research was conducted in the absence of any commercial or financial relationships that could be construed as a potential conflict of interest.

## References

- Wang, S.; Zeng, T.; Wen, X.; Xu, H.; Fan, F.; Wang, X.; Tian, G.; Liu, S.; Liu, P.; Wang, C.; et al. Optimized Lithium Ion Coordination via Chlorine Substitution to Enhance Ionic Conductivity of Garnet-Based Solid Electrolytes. *Small* **2024**, *20*, 2309874. [[CrossRef](#)] [[PubMed](#)]
- Wang, X.; Du, D.; Yan, Y.; Ren, L.; Xu, H.; Wen, X.; Zeng, T.; Tian, G.; Liu, S.; Fan, F.; et al. Molecular Cleavage Strategy Enabling Optimized Local Electron Structure of Co-Based Metal-Organic Framework to Accelerate the Kinetics of Oxygen Electrode Reactions in Lithium-Oxygen Battery. *Energy Storage Mater.* **2023**, *63*, 103033. [[CrossRef](#)]
- Xu, H.; Wang, X.; Tian, G.; Fan, F.; Wen, X.; Liu, P.; Shu, C. Manipulating Electron Delocalization of Metal Sites via a High-Entropy Strategy for Accelerating Oxygen Electrode Reactions in Lithium-Oxygen Batteries. *ACS Nano* **2024**, *18*, 27804–27816. [[CrossRef](#)]
- Park, M.H.; Kim, M.G.; Joo, J.; Kim, K.; Kim, J.; Ahn, S.; Cui, Y.; Cho, J. Silicon Nanotube Battery Anodes. *Nano Lett.* **2009**, *9*, 3844–3847. [[CrossRef](#)] [[PubMed](#)]

5. Liu, J.; Kopold, P.; van Aken, P.A.; Maier, J.; Yu, Y. Energy Storage Materials from Nature through Nanotechnology: A Sustainable Route from Reed Plants to a Silicon Anode for Lithium-Ion Batteries. *Angew. Chem. Int. Ed.* **2015**, *54*, 9632–9636. [[CrossRef](#)] [[PubMed](#)]
6. Kim, H.; Han, B.; Choo, J.; Cho, J. Three-Dimensional Porous Silicon Particles for Use in High-Performance Lithium Secondary Batteries. *Angew. Chem. Int. Ed.* **2008**, *47*, 10151–10154. [[CrossRef](#)]
7. Obrovac, M.N.; Christensen, L. Structural Changes in Silicon Anodes during Lithium Insertion/Extraction. *Electrochem. Solid-State Lett.* **2004**, *7*, A93. [[CrossRef](#)]
8. Zhao, R.; Wang, S.; Liu, D.; Liu, Y.; Lv, X.; Zeng, X.; Li, B. Effect of Fluoroethylene Carbonate on Solid Electrolyte Interphase Formation of the SiO/C Anode Observed by in Situ Atomic Force Microscopy. *ACS Appl. Energy Mater.* **2021**, *4*, 492–499. [[CrossRef](#)]
9. Zhang, C.; Wang, F.; Han, J.; Bai, S.; Tan, J.; Liu, J.; Li, F. Challenges and Recent Progress on Silicon-Based Anode Materials for Next-Generation Lithium-Ion Batteries. *Small Struct.* **2021**, *2*, 2100009. [[CrossRef](#)]
10. Chen, T.; Wu, J.; Zhang, Q.; Su, X. Recent Advancement of SiOx Based Anodes for Lithium-Ion Batteries. *J. Power Sources* **2017**, *363*, 126–144. [[CrossRef](#)]
11. Greenwood, M.; Wentker, M.; Leker, J. A Bottom-up Performance and Cost Assessment of Lithium-Ion Battery Pouch Cells Utilizing Nickel-Rich Cathode Active Materials and Silicon-Graphite Composite Anodes. *J. Power Sources Adv.* **2021**, *9*, 100055. [[CrossRef](#)]
12. Choi, J.W.; Aurbach, D. Promise and Reality of Post-Lithium-Ion Batteries with High Energy Densities. *Nat. Rev. Mater.* **2016**, *1*, 16013. [[CrossRef](#)]
13. Lu, Y.; Tu, Z.; Shu, J.; Archer, L.A. Stable Lithium Electrodeposition in Salt-Reinforced Electrolytes. *J. Power Sources* **2015**, *279*, 413–418. [[CrossRef](#)]
14. Heiskanen, S.K.; Kim, J.; Lucht, B.L. Generation and Evolution of the Solid Electrolyte Interphase of Lithium-Ion Batteries. *Joule* **2019**, *3*, 2322–2333. [[CrossRef](#)]
15. Ming, J.; Cao, Z.; Wu, Y.; Wahyudi, W.; Wang, W.; Guo, X.; Cavallo, L.; Hwang, J.Y.; Shamim, A.; Li, L.J.; et al. New Insight on the Role of Electrolyte Additives in Rechargeable Lithium Ion Batteries. *ACS Energy Lett.* **2019**, *4*, 2613–2622. [[CrossRef](#)]
16. Jiang, F.; Sun, Y.; Zhang, K.; Liu, Y.; Feng, X.; Xiang, H. SiOx/C Anodes with High Initial Coulombic Efficiency through the Synergy Effect of Pre-Lithiation and Fluoroethylene Carbonate for Lithium-Ion Batteries. *Electrochim. Acta* **2021**, *398*, 139315. [[CrossRef](#)]
17. Gong, S.; Lee, Y.; Choi, J.; Lee, M.; Chung, K.Y.; Jung, H.G.; Jeong, S.; Kim, H.S. In Situ Mesopore Formation in SiOx Nanoparticles by Chemically Reinforced Heterointerface and Use of Chemical Prelithiation for Highly Reversible Lithium-Ion Battery Anode. *Small* **2023**, *19*, 2206238. [[CrossRef](#)]
18. Xu, S.; Hou, X.; Wang, D.; Zuin, L.; Zhou, J.; Hou, Y.; Mann, M. Insights into the Effect of Heat Treatment and Carbon Coating on the Electrochemical Behaviors of SiO Anodes for Li-Ion Batteries. *Adv. Energy Mater.* **2022**, *12*, 2200127. [[CrossRef](#)]
19. Chen, L.; Wang, K.; Xie, X.; Xie, J. Effect of Vinylene Carbonate (VC) as Electrolyte Additive on Electrochemical Performance of Si Film Anode for Lithium Ion Batteries. *J. Power Sources* **2007**, *174*, 538–543. [[CrossRef](#)]
20. Liu, S.; Shu, C.; Yan, Y.; Ren, L.; Du, D.; Zeng, T.; Wen, X.; Xu, H.; Zhao, C.; Wang, X.; et al. Regulating Solvation Environment of Li Ions via High Donor Number Anions for High-Performance Li-Metal Batteries. *Chem. Eng. J.* **2022**, *450*, 138369. [[CrossRef](#)]
21. Liu, S.; Yu, X.; Yan, Y.; Zeng, T.; Wang, X.; Tian, G.; Wang, C.; Wang, S.; Zeng, Y.; Shu, C. Dendrite-Free Lithium Deposition Enabled by Interfacial Regulation via Dipole-Dipole Interaction in Anode-Free Lithium Metal Batteries. *Energy Storage Mater.* **2023**, *62*, 102959. [[CrossRef](#)]
22. Wang, C.; Ouyang, T.; Wang, X.; Liu, S.; Tian, G.; Fan, F.; Liu, P.; Wang, S.; Zeng, C.; Shu, C. Accelerating Lithium Ion Transport via Increasing the Entropy of the Electrolyte for Stable Lithium Metal Batteries. *J. Energy Chem.* **2024**, *99*, 384–392. [[CrossRef](#)]
23. Shen, Y.; Cao, Z.; Wu, Y.; Cheng, Y.; Xue, H.; Zou, Y.; Liu, G.; Yin, D.; Cavallo, L.; Wang, L.; et al. Catalysis of Silica-Based Anode (de-)Lithiation: Compositional Design within a Hollow Structure for Accelerated Conversion Reaction Kinetics. *J. Mater. Chem. A* **2020**, *8*, 12306–12313. [[CrossRef](#)]
24. Wang, H.; Cai, W.; Wang, S.; Li, B.; Yang, Y.; Li, Y.; Wu, Q.H. Fabrication of Helical SiO<sub>2</sub>@Fe-N Doped C Nanofibers and Their Applications as Stable Lithium Ion Battery Anodes and Superior Oxygen Reduction Reaction Catalysts. *Electrochim. Acta* **2020**, *342*, 136107. [[CrossRef](#)]
25. Kang, T.; Tan, J.; Li, X.; Liang, J.; Wang, H.; Shen, D.; Wu, Y.; Huang, Z.; Lu, Y.; Tong, Z.; et al. Armoring Si-Oxwith a Conformal LiF Layer to Boost Lithium Storage. *J. Mater. Chem. A* **2021**, *9*, 7807–7816. [[CrossRef](#)]
26. Yamada, Y.; Iriyama, Y.; Abe, T.; Ogumi, Z. Kinetics of Electrochemical Insertion and Extraction of Lithium Ion at SiO. *J. Electrochem. Soc.* **2010**, *157*, A26. [[CrossRef](#)]
27. Tao, H.C.; Fan, L.Z.; Mei, Y.; Qu, X. Self-Supporting Si/Reduced Graphene Oxide Nanocomposite Films as Anode for Lithium Ion Batteries. *Electrochim. Commun.* **2011**, *13*, 1332–1335. [[CrossRef](#)]
28. Demczyk, B.G.; Wang, Y.M.; Cumings, J.; Hetman, M.; Han, W.; Zettl, A.; Ritchie, R.O. Direct Mechanical Measurement of the Tensile Strength and Elastic Modulus of Multiwalled Carbon Nanotubes. *Mater. Sci. Eng. A* **2002**, *334*, 173–178. [[CrossRef](#)]
29. Xu, K. Nonaqueous Liquid Electrolytes for Lithium-Based Rechargeable Batteries. *Chem. Rev.* **2004**, *104*, 4303–4417. [[CrossRef](#)]
30. Zhang, X.-Q.; Cheng, X.-B.; Chen, X.; Yan, C.; Zhang, Q.; Zhang, X.; Cheng, X.; Chen, X.; Yan, C.; Zhang, Q. Fluoroethylene Carbonate Additives to Render Uniform Li Deposits in Lithium Metal Batteries. *Adv. Funct. Mater.* **2017**, *27*, 1605989. [[CrossRef](#)]

31. Antoun, G.; Girard, A.; Tilloccher, T.; Lefaucheux, P.; Faguet, J.; Maekawa, K.; Cardinaud, C.; Dussart, R. Quasi In Situ XPS on a SiOxFy Layer Deposited on Silicon by a Cryogenic Process. *ECS J. Solid State Sci. Technol.* **2022**, *11*, 013013. [[CrossRef](#)]
32. Philippe, B.; Dedryvère, R.; Allouche, J.; Lindgren, F.; Gorgoi, M.; Rensmo, H.; Gonbeau, D.; Edström, K. Nanosilicon Electrodes for Lithium-Ion Batteries: Interfacial Mechanisms Studied by Hard and Soft X-Ray Photoelectron Spectroscopy. *Chem. Mater.* **2012**, *24*, 1107–1115. [[CrossRef](#)]
33. Jiao, M.; Wang, Y.; Ye, C.; Wang, C.; Zhang, W.; Liang, C. High-Capacity SiO<sub>x</sub> ( $0 \leq x \leq 2$ ) as Promising Anode Materials for next-Generation Lithium-Ion Batteries. *J. Alloys Compd.* **2020**, *842*, 155774. [[CrossRef](#)]
34. Nguyen, C.C.; Choi, H.; Song, S.-W. Roles of Oxygen and Interfacial Stabilization in Enhancing the Cycling Ability of Silicon Oxide Anodes for Rechargeable Lithium Batteries. *J. Electrochem. Soc.* **2013**, *160*, A906–A914. [[CrossRef](#)]
35. Song, J.W.; Nguyen, C.C.; Song, S.W. Stabilized Cycling Performance of Silicon Oxide Anode in Ionic Liquid Electrolyte for Rechargeable Lithium Batteries. *RSC Adv.* **2012**, *2*, 2003–2009. [[CrossRef](#)]
36. Nguyen, C.C.; Song, S.W. Interfacial Structural Stabilization on Amorphous Silicon Anode for Improved Cycling Performance in Lithium-Ion Batteries. *Electrochim. Acta* **2010**, *55*, 3026–3033. [[CrossRef](#)]
37. Zhang, Q.; Pan, J.; Lu, P.; Liu, Z.; Verbrugge, M.W.; Sheldon, B.W.; Cheng, Y.T.; Qi, Y.; Xiao, X. Synergetic Effects of Inorganic Components in Solid Electrolyte Interphase on High Cycle Efficiency of Lithium Ion Batteries. *Nano Lett.* **2016**, *16*, 2011–2016. [[CrossRef](#)]

**Disclaimer/Publisher's Note:** The statements, opinions and data contained in all publications are solely those of the individual author(s) and contributor(s) and not of MDPI and/or the editor(s). MDPI and/or the editor(s) disclaim responsibility for any injury to people or property resulting from any ideas, methods, instructions or products referred to in the content.